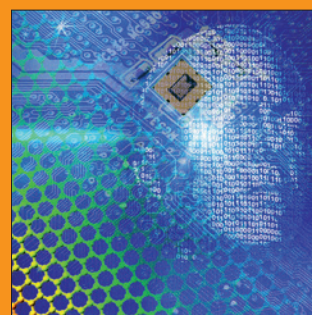
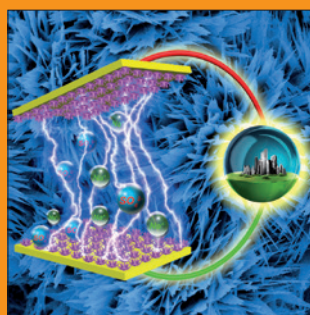
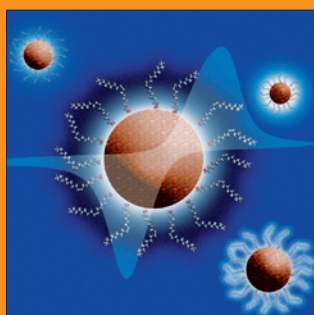
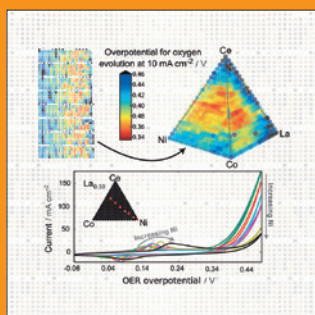
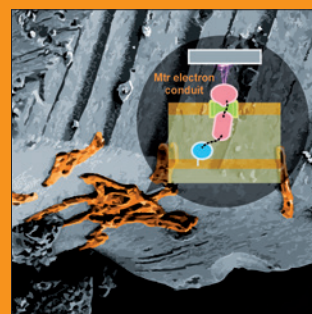
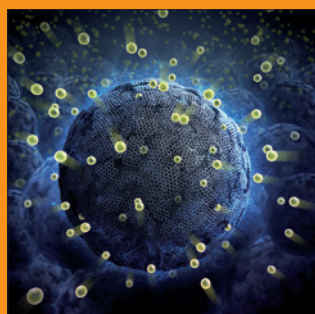
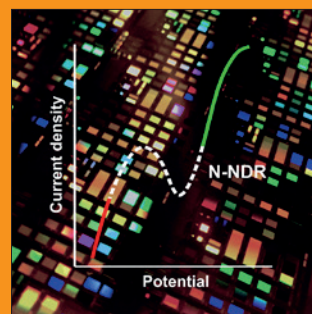
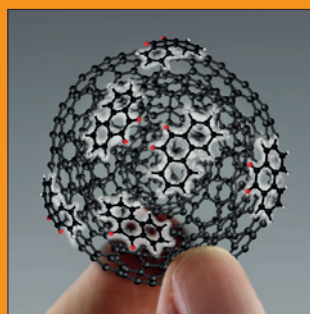
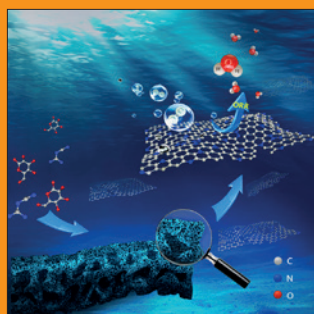
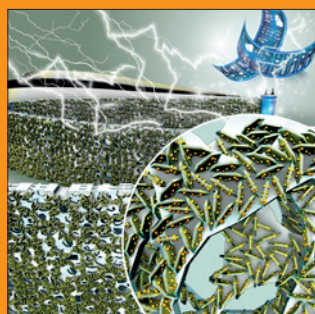


FUNDAMENTALS & APPLICATIONS

CHEMELECTROCHEM

ANALYSIS & CATALYSIS, BIO & NANO, ENERGY & MORE



Reprint

A Journal of



WILEY-VCH

www.chemelectrochem.org

Synergistic Catalytic Effect of Ion Tunnels with Polar Dopants to Boost the Electrochemical Kinetics for High-Performance Sulfur Cathodes

Jing Zhang,^[a] Caiyin You,^{*[a]} Jian Wang,^[b] Shaohua Guo,^[a] Weihua Zhang,^[a] Rong Yang,^[c] and Ping Fu^[d]

Rechargeable lithium–sulfur (Li–S) batteries with high areal capacity are hindered by the ion/electron pathway and sluggish reaction kinetics of sulfur species, resulting from high energy barriers. Inspired by the nature of biomass and efficient nutrition transfer, we present a high-performance sulfur cathode based on nanocarbon tunnels with natural polar catalytic sites. The inherited tunnels can propel lithium-ion transport across the interface to reach the active materials and the

interior heteroatom dopants provide abundant catalytic sites to further reduce the energy barriers. The as-fabricated sulfur cathode displays much higher rate performance of 565 mA h g^{-1} at 6 C and a low decay rates of 0.029% per cycle for 2000 cycles at 3 C. Most importantly, a high initial areal capacity of 5.1 mA h cm^{-2} with enhanced loading up to 5.8 mg cm^{-2} at 1 C is achieved, corresponding to volumetric capacity of 638 Ah L^{-1} .

1. Introduction

With the increase of energy demands, environmental problems and the rise in global warming, the development of rechargeable batteries with high energy density is of great interest in recent years.^[1,2] The lithium–sulfur (Li–S) batteries represent the promising solutions to satisfy portable storage devices and hybrid electric vehicles due to the competitively theoretical energy density (2600 Wh kg^{-1}), three to fivefold higher than Li-ion batteries.^[3,4] However, the commercial application of Li–S batteries is still challenged by the low utilization of sulfur resulting from sluggish reaction kinetics and the immigration of polysulfides.^[5–10] These issues significantly deteriorate electrochemical performances of the batteries, including low coulombic efficiency, fast capacity fade and short cycling life.

The design and fabrication of advanced sulfur cathodes based on carbon materials are widely accepted to be the workable way to conquer those problems due to their desirable features including excellent conductivity and chemical

stability.^[11–23] With the in-depth research, the simply combination of excellent conductivity and adsorption sites within the carbon host is not good enough to satisfy the increasing demands of rapid charge/discharge for developing fast and long cycling life of the batteries. As is well known, electron transfer and lithium ion transport across the interfaces are quite decisive to the battery performance. Recent literatures have evidenced that the fast electron transfer is critical for the reaction kinetics closely related to the rate capability of the batteries.^[24–26] However, little reports pay attention to the ion transport across the interface, which is quite important in the high rate performance. To boost the electrochemical kinetics, two general approaches should have been employed. One accessible strategy is constructing fast ion tunnels in the conductive carbon matrix, which could continuously pump lithium ions to accelerate the conversions of sulfur species. Another is the polar catalytic sites that is able to decrease the energy barrier of interconversions among sulfur species, leading to a superb redox conversion efficiency. Till now, it still remains challenging to develop carbon materials with tunnels at high yield through simple steps with low cost and environmental benignity. Natural biomasses with tube-like branches in leaves for passing the nutrition from bottom root for photosynthesis^[27] can provide tunnels for fast electrolyte infiltration and ion/electron transfer after carbonization. Meanwhile, the inherent polar heteroatom dopants (S, N, B, P and F) can supply potential catalytic effect to effectively propel the redox kinetics^[28,29] without sacrificing the energy density of Li–S batteries in comparison to introducing metal-based additives.^[30] The abundant dopants also strengthen the ability of anchoring polysulfides chemically and alleviate shuttle effect.^[11,31]

Herein, we inherit the structural merits of the tube-like branches working for biological nutrition transfer in rice straw to construct the functional ionic/electron tunnels with polar catalytic sites. The tube-like branches are able to render the

[a] J. Zhang, Prof. C. You, Prof. S. Guo, Prof. W. Zhang
School of Materials Science and Engineering
Xi'an University of Technology
Xi'an 710048, P. R. China
E-mail: caiyinyou@xaut.edu.cn

[b] J. Wang
i-Lab, Suzhou Institute of Nano-Tech and Nano-Bionics
Chinese Academy of Sciences
Suzhou, Jiangsu, 215123, P. R. China

[c] Prof. R. Yang
School of Sciences, Xi'an University of Technology
Xi'an 710048, P. R. China

[d] Prof. P. Fu
Hubei Key Laboratory of Plasma Chemistry and Advanced Materials
School of Materials Science and Engineering
Wuhan Institute of Technology
Wuhan 430073, P. R. China

Supporting information for this article is available on the WWW under <https://doi.org/10.1002/celc.201901360>

carbon tunnels for electrolyte penetration and ion transport for boosting the electrochemical reaction kinetics, which also maintains a continuous access to the electron transfer. Meanwhile, the inherent heteroatom polar sites show the catalytic ability to reduce the energy barrier and strengthen the chemisorption capability synergistically without sacrificing the energy density. The as-prepared cathode based on this structure realizes a high-rate performance (564 mAh g^{-1} at 6 C) and long lifespan of 2000 cycles at 3 C. Even under a high areal sulfur loading up to 5.8 mg cm^{-2} , the cell can still work at 1 C (9.74 mAh cm^{-2}) and initially delivers high areal capacity of 5.1 mAh cm^{-2} . These results provide a unique perspective of taking advantage of the renewable biomaterials to catalyze the interconversions for developing high-performance Li-S batteries.

2. Results and Discussion

Figure 1 schematically presents the structural merits of the tunnels derived from the biological nutrition transfer pathway in the rice straw leaves. As shown in Figure 1, the carbon tunnels can provide smooth passages to ensure fast transport of lithium ions and sufficient electrolyte infiltration. At the same time, the conductive porous tunnel walls can maintain a continuous and convenient access to the electron transfer. Moreover, the naturally doped heteroatoms on the surface of the tunnels could offer numerous active sites to anchor the polysulfides tightly and catalyze the interconversions of the sulfur species. Benefiting from the ion transport tunnels and the surficial catalytic sites, the aim of fast redox kinetics and low polysulfides dissolution are achieved. These natural features will be verified thoroughly in the following characterizations.

The morphologies of the natural heteroatom-doped and activated carbon (NHAC) were characterized by scanning electron microscopy (SEM) and transmission electron microscopy (TEM). As shown in Figure 2a, the micro-architecture tunnel is obviously observed and the carbon tunnels are uniformly distributed among the porous sheet structures (Figure S1). Meanwhile, affluent mesopores are also observed on

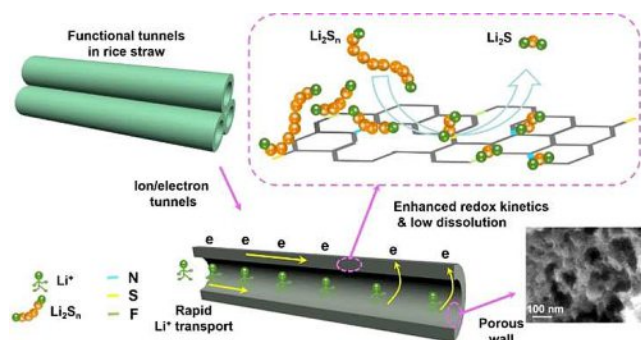


Figure 1. Strategy of rapid ion tunnels with natural catalytic sites (through the naturally doped heteroatoms N, S and F) in sulfur cathode: The multifunctional tunnels inheriting from the branches of the rice straw including fast electron/ion transfer and actively catalytic effect to enhance the redox kinetic and polysulfide anchoring.

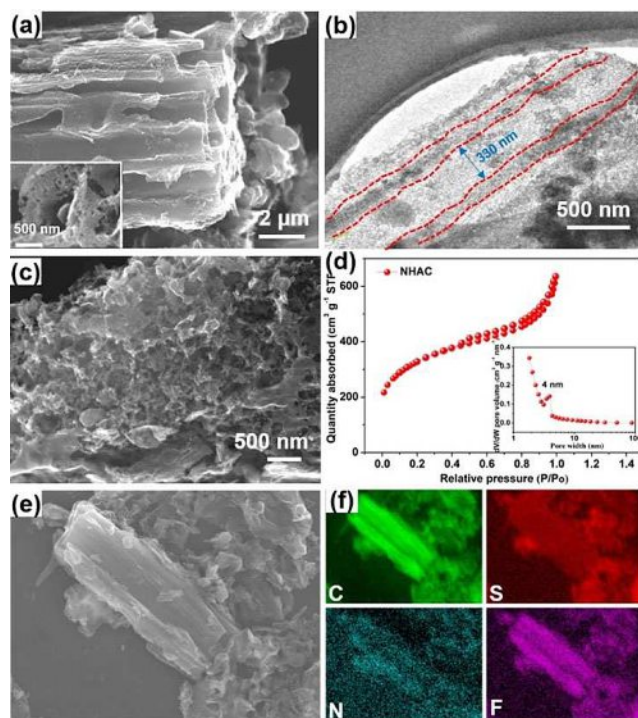


Figure 2. Characterization of pore morphology and structure of the NHAC: a) SEM image of carbon micro-tunnels and the inset of the affluent mesopores on the tunnel walls; b) TEM image of carbon micro-tunnels; c) SEM image of the porous carbon sheet structure; d) pore-size distribution for NHAC (the inset of the N_2 adsorption/desorption isotherms); e) selected SEM image of the porous NHAC for elemental mapping analyses and f) corresponding EDS elemental mapping image of carbon, sulfur, nitrogen and fluorine.

the tube walls (inset of Figure 2a). Further, the TEM image (Figure 2b) presents the typical tunnels with diameter around 500 nm and porous wall. Such tunnel structure can provide a large number of pathways for lithium ion transfer and electrolyte infiltration to reach the active materials. Figure 2c displays the high-resolution of the carbon sheet as a porous structure with interconnected mesopores. All of the mesopores are good catchers of polysulfides and can supply affluent space for electrochemical reactions. Nitrogen adsorption-desorption isotherms were carried out to examine the porous structure of the NHAC. The NHAC shows type IV isotherms with hysteresis loop in the relative pressure range from 0.4 to 1 P/P_0 ^[23], as revealed in the inset of Figure 2d. The NHAC possesses a large specific surface area of $1187 \text{ m}^2 \text{ g}^{-1}$ (against $191 \text{ m}^2 \text{ g}^{-1}$ of ABT and $79 \text{ m}^2 \text{ g}^{-1}$ of AB in Figure S2a and b), which may be beneficial for exposing more active sites for trapping polysulfides. The pore size distribution calculated by Barrett-Joyner-Halenda (BJH) equation in Figure 2d shows a sharp peak centered at about 4 nm, further revealing many mesoporous pores in NHAC. The elemental energy dispersive spectra (EDS) elemental mappings display the similar color morphology of elemental C, S, N and F, implying the homogeneous distribution of heteroatoms within the NHAC, as illustrated in Figure 2e and f.

The X-ray diffraction (XRD) patterns of NHAC before and after sulfur loading (named as NHAC-S) are presented in Figure 3a. The NHAC exhibits the broad diffraction peaks

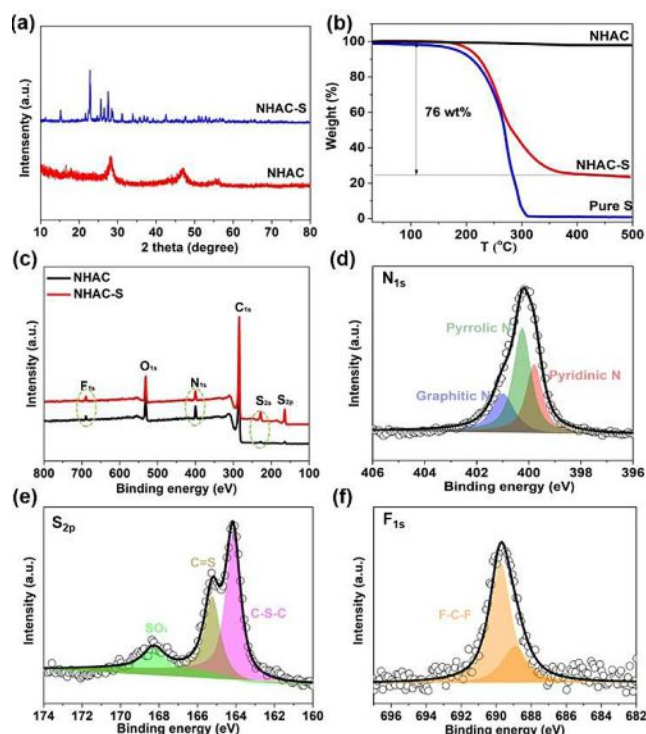


Figure 3. The evidence of natural heteroatom-doping in NHAC: a) XRD patterns of NHAC and NHAC–S composite; b) TG curves of NHAC–S composite; c) XPS analysis spectra of NHAC and NHAC–S composites; high-resolution d) N_{1s} , e) S_{2p} and f) F_{1s} spectra in NHAC.

around 28° , 47° and 56° , which are almost consistent with the pattern of graphite carbon (JCPDS NO.75-2078) except a slightly positive shift. The shift of the peaks suggests the possibility of the implantation of heteroatoms into the carbon lattices. After sulfur imbedding, the NHAC–S composite mainly presents the crystal peaks of sulfur (Figure 3a). Figure 3b shows that the sulfur content in NHAC–S is measured up to 76 wt% by thermogravimetric analysis (TGA). In addition, the sulfur in NHAC–S composite evaporates completely around 380°C while pure sulfur evaporates completely at 310°C , indicating that the sulfur is confined by strong capillary force of mesopores in the NHAC. And the sulfur is homogeneously imbedded in the NHAC frameworks without detection of apparent agglomerates (Figure S3). After sulfur infiltration, the NHAC–S composite exhibits lower specific surface area ($8.42\text{ m}^2\text{g}^{-1}$) and pore volume than the NHAC after sulfur infusion (76 wt%).

The Raman spectra of NHAC (Figure S4) displays the well-known D-band peak (1321 cm^{-1}) and G-band peak (1588 cm^{-1}), respectively. The G-band peak presents the characteristic of partial graphitization, which is favorable for promoting the electronic conductivity of NHAC. The X-ray photoelectron spectroscopy (XPS) was applied to analyze the surface chemistry of the NHAC. Figure 3c–f reveal the XPS spectra of NHAC, which is the further evidence of the natural elemental doping. The full XPS spectrum of NHAC in Figure 3c indicates the diverse heteroatom-doping with overall doping contents up to 6.92 at % (1.07 at% for F, 0.86 at% for S and 4.99 at% for N). The carbon atoms become more positively charged through heteroatoms

doping due to the larger electronegativity of the common heteroatoms than carbon atom ($F > N > S > C$). The redistribution of charges conduces to the polarization of the doping sites, which facilitates the trapping of polysulfides through forming favorable bonds between Li^+ and heteroatoms.^[32] Such a high level of elemental doping in the NHAC can offer a high density of functional sites for polysulfide trapping chemically and catalytic conversion. The high-resolution of C_{1s} peak of NHAC (Figure S5) displays peaks at 285.5, 286.3 and 288.1 eV, assigning to C–S, C–N–C and C–F species, respectively.^[32–34] As displayed in Figure 3d, the high-resolution N_{1s} spectrum indicates the presence of graphitic N, pyrrolic N, and pyridinic N at 401.1, 400.3 and 399.8 eV. The high-resolution S_{2p} spectrum in Figure 3e demonstrates the existence of three components centered at 164.1 and 165.2, 168.3 eV, attributing to the C–S–C and C=S, and SO_x species, respectively. As for the high-resolution F_{1s} spectrum in Figure 3f, both the peaks at 688.8 and 689.7 eV are ascribed to C–F bonds.^[33,34] These results strongly suggest the evidence of natural polar sites in the tunnel matrix, which is beneficial for catalysis and chemisorption for polysulfides.

To demonstrate the effects of chemisorption and catalysis, the controllable sample of larger carbon tunnels stripped from the straw with acetylene black (named as ABT) and acetylene black (AB) were also made. Optical and ultraviolet visible experiments were carried out. As shown in the inset of Figure 4a, the sample with NHAC host shows colorless in contrast to others (ABT, AB and control sample) after a long enough adsorption by the hosts. Furthermore, the residual concentration of polysulfides in the solutions were measured by ultraviolet visible (UV-vis), as demonstrated in Figure 4a. NHAC indicates the weakest absorbance around 410 nm^{-1} , implying the strongest absorptivity of NHAC towards polysulfides than ABT and AB (adsorption efficiency: 95 % vs. 74 % vs. 32 %). Heteroatom-doped carbon materials also act as the electrocatalysts due to the high electron affinity of the doped species.^[28–30] To evaluate the catalytic effect on the electrochemical conversion of polysulfides, cyclic voltammetry (CV) curves using symmetric cells based on pristine NHAC, AB and ABT, respectively, with $0.2\text{ mol L}^{-1}\text{ Li}_2\text{S}_6$ electrolyte were carried out. As displayed in Figure 4b, the two pairs of redox peaks can be attributed to the reversible electrochemical interconversions of $\text{S}_8 \rightleftharpoons \text{S}_6^{2-} \rightleftharpoons \text{Li}_2\text{S}$, due to the only electrochemically active species of Li_2S_6 in the electrolyte. The two reduction peaks at -0.295 V ($\text{S}_6^{2-} \rightarrow \text{Li}_2\text{S}$) and 0.073 V ($\text{S}_8 \rightarrow \text{S}_6^{2-}$), and two distinct oxidation peaks around -0.082 V ($\text{Li}_2\text{S} \rightarrow \text{S}_6^{2-}$) and 0.304 V ($\text{S}_6^{2-} \rightarrow \text{S}_8$) were recorded.^[35] In contrast to AB and ABT electrode, the NHAC working electrode presents the narrowest peak potential differences, largest peak current and area, corresponding to the highest catalytic efficiency.^[36] The electrochemical impedance spectroscopy (EIS) in Figure 4c has also displayed the smallest charge transfer resistance of the NHAC electrode among the symmetric cells ($2.954\text{ }\Omega$ vs. $5.294\text{ }\Omega$ vs. $6.401\text{ }\Omega$) due to the best conductivity (Table S1). In principle, the surface chemistry of the nanocarbon has a relationship with the nucleation and growth of the Li_2S . The Li_2S nucleation test was performed on cells with polysulfide catholyte. As shown in

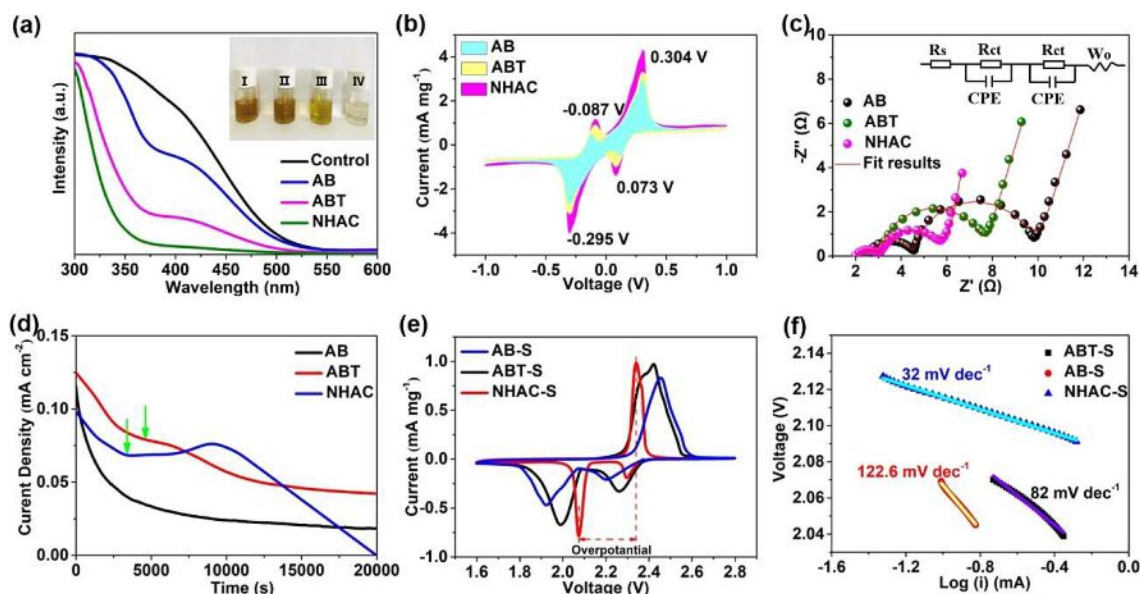


Figure 4. Synergistically chemisorption and catalytic effects in electrochemical conversion: a) UV/Vis spectra of the polysulfide solution after exposure to the different adsorbents and the inset photo image of polysulfide solution after exposure to the adsorbents for 8 h; I) contrast, II) AB, III) ABT and IV) NHAC. b) CV plots of the symmetric cells with NHAC, ABT and AB in $0.2 \text{ mol L}^{-1} \text{ Li}_2\text{S}_6$ at the scan rate of 0.5 mV s^{-1} ; c) EIS comparison among the AB, ABT and NHAC symmetric cells and the inset of the used equivalent circuit; d) current-time profile for potentiostatic discharge in polysulfide catholyte; e) first cycle of the CV profiles of the three cathodes at the scan rate of 0.1 mV s^{-1} ; f) Tafel plots for the corresponding second reduction conversion of the three cathodes.

Figure 4d, the response of the Li_2S is earlier and the current peaks is higher in the NHAC electrode over that on the ABT electrode (indicated by the green arrows). Meanwhile, the AB electrode shows no characteristic nucleation of Li_2S . These results demonstrate the ion tunnel with polar elements doping could induce the initial nucleation of Li_2S .^[37]

After the sulfur loading, the CV measurements and Tafel plots of these cathodes (Figure 4e and f) were carried out to further verify the catalytic activity on the reaction kinetics of the cathode. As shown in Figure 4e, two pairs of cathodic and anodic peaks are clearly observed on the three cathodes. The NHAC-S cathode presents significantly lowest charge/discharge overpotential (270 vs. 430 vs. 530 mV), implying the high reaction activity. The enhanced catalytic kinetic behavior can be further evaluated by the Tafel behavior derived from the CV measurement. The exchange current density values derived from a Tafel plot is related to the electrochemical reaction rate as revealed in the Butler-Volmer equation.^[38,39] The Tafel plots of the NHAC-S cathode in Figure 4f displays the smallest Tafel plot slope of 32 mV dec^{-1} (Table S2), strongly lower than that of ABT-S (82 mV dec^{-1}) and AB-S ($122.6 \text{ mV dec}^{-1}$). The increased exchange current density and lower Tafel plot slope imply the lower energy barrier and fast kinetics of the interconversions among sulfur species in NHAC-S cathode. Combining all the results of synergistical chemisorption and catalytic analysis, the electrochemical reaction kinetics of polysulfides is enhanced indeed by the prepared ion tunnel.

It is well known that the catalytic effect on the reaction between Li_2S_x ($4 \leq x \leq 8$) and $\text{Li}_2\text{S}/\text{Li}_2\text{S}_2$ is still closely connected with the lithium ion transport rate. The EIS and CV measurements were carried out to understand the ion transfer kinetics

with tunnels. The EIS comparison of fresh cathodes performed at open-circuit voltage is displayed in Figure 5a. All of the EIS plots are composed of a semicircle within the range of medium to high frequency and an oblique line in the low frequency region. As revealed in Figure 5a, the NHAC-S cathode displays the smallest resistance of 24 Ω against 122 Ω of ABT-S and 231 Ω of AB-S, implying the rapid charge transfer. In addition, the sloped line in Figure 5a represents the Warburg impedance, which can be associated with mobility of lithium ion in the cathode. And the real part (Z') of the impedance is plotted as the function of the reciprocal exponential ($\omega^{-1/2}$) of the lower angular frequency (Figure 5b). The slope of σ can be obtained from the fitting lines. Smaller slope (σ) of the line corresponds to much larger lithium ion diffusion coefficients according to the ion diffusion coefficient equation [Eq. (1)].^[40]

$$D = \frac{R^2 T^2}{2A^2 n^4 F^4 C^2 \sigma^2} \quad (1)$$

Where R is the gas constant ($8.314 \text{ J K}^{-1} \text{ mol}^{-1}$), T is the experimental temperature (298 K), A is the surface area of the cathode, n is the number of electrons per molecule during oxidation, F is the Faraday's constant (96500 C mol^{-1}), C is the initial concentration of lithium ion in the cathode. As shown in Figure 5b, the NHAC-S cathode presents the smallest slope (σ), implying fastest lithium ion diffusion coefficient for acceleration of lithium ion transfer. Furthermore, the CV measurement under various scan rate was also carried out to get deeper insight. As depicted by Figure 5c and S5, each CV curve displays two cathodic peaks and an anodic peak. The cathodic peaks are related to the multi-step reaction of active sulfur. And the

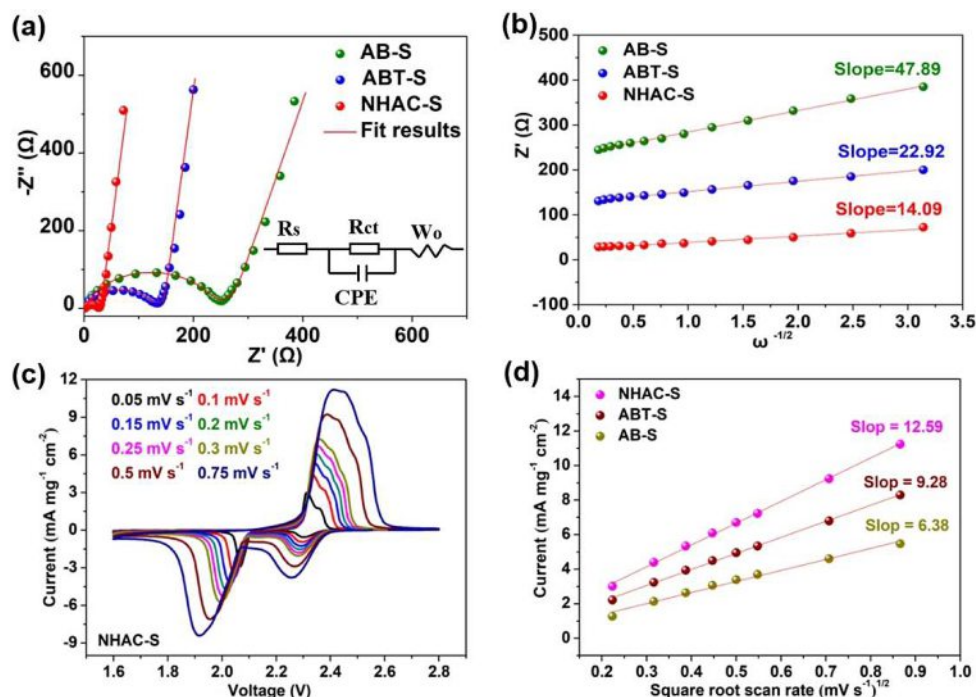


Figure 5. Confirming the improved Li ion transfer through tunnels: a) EIS comparisons of NHAC-S, ABT-S and AB-S cathodes and the inset of the related equivalent circuit; b) plots of the linear relationship between the real part of the impedance and the reciprocal exponential ($-1/2$) at the lower angular frequency; c) representative CV curves of NHAC-S cathode depending on different scan rate; d) plots of the anodic peak currents versus the square root of the scan rates derived from scan rate depending CV.

anodic peak corresponds to the oxidation of polysulfides to sulfur. The anodic peak current values are linearly related to the square root of the scanning rate in terms of the classical Randles-Sevcik equation [Eq. (2)]:^[36,41]

$$i_p = 0.4463nFAC \left(\frac{nFvD}{RT} \right)^{1/2} \quad (2)$$

Where i_p is current maximum of anodic peak depending on the scan rate, n is the number of electrons transferred in the redox event (usually 1), A is electrode area, F is Faraday's constant (96500 C mol^{-1}), D is diffusion coefficient, C is concentration, v is scan rate, R is Gas constant and T is temperature (298 K). The Figure 5d reveals the linear relation between the square root of the scanning rate and the anodic peak current of the cathode obtained from the CV in Figure 5c and Figure S6a and b. The slope of the line is proportional to the lithium ion diffusion coefficient. With rapid ion tunnels, the NHAC-S cathode displays the largest line slope and lithium ion diffusion coefficient among the three cathodes (Figure 5d and Figure S6c). The improvement in the lithium ion transfer by the tunnels should be related to the promoted reaction kinetics.

The fast reaction kinetics are undoubtedly attributed to the catalytic effect of the polar sites and fast ion transfer through the ionic tunnels. As expected, a good rate performance for the NHAC-S cathode is achieved in Figure 6a. The charge/discharge-voltage profile of NHAC-S cathode maintains the similar shape at different current rate. These charge/discharge-voltage curves consist of two obvious discharge plateaus and

one charge plateau, in agreement with the CV curve in Figure 5c. The NHAC-S cathode in Figure 6b initially delivers a discharge capacity of 1201 mAh g^{-1} at 0.05 C . Upon further cycling at $0.1, 0.2, 1, 2, 4$ and 6 C , it exhibits a reversible capacity of $1153, 998, 812, 738, 624$ and 564 mAh g^{-1} , respectively. The cathode regains a reversible capacity of 868 mAh g^{-1} when it recovers to 0.2 C , indicating excellent reversibility. In sharply contrast, the ABT-S cathode with ion tunnel exhibit a much higher rate capacity than AB-S cathode especially at high rate of 6 C but still much lower than NHAC-S (Figure 6b). As well known, the rate reversibility of sulfur cathode is influenced by the conversion rate and the transport rate of ions during lithiation/delithiation. The NHAC-S displays the smallest delithiation potential barrier of 2.22 V against 2.27 V of ABT-S and 2.32 V of AB-S, directly reflecting the propelling effect of the rapid ion transfer and catalytic effect originated from the tunnels in the interior of Li_2S (Figure 6c).

Excellent high-rate cycling performance is the long-pursued aim for the massive practical application of Li-S based batteries. As can be seen from Figure 6d, the NHAC-S cathode delivers the initially discharge capacity of 755 mAh g^{-1} at 2 C , which is about 7 times higher than the AB-S cathode. It still maintains reversible discharge capacity of 584 mAh g^{-1} after 500 cycles, much higher than the controllable ones (258 mAh g^{-1} and 104 mAh g^{-1}). Even increased the rate to 3 C , the NHAC-S cathode still exhibits an excellent long-term lifespan with a decay rates as low as 0.029% per cycle for 2000 cycles in Figure S7a. The discharge/charge plateaus are stably remained (Figure S7b), suggesting the excellent structural stability and

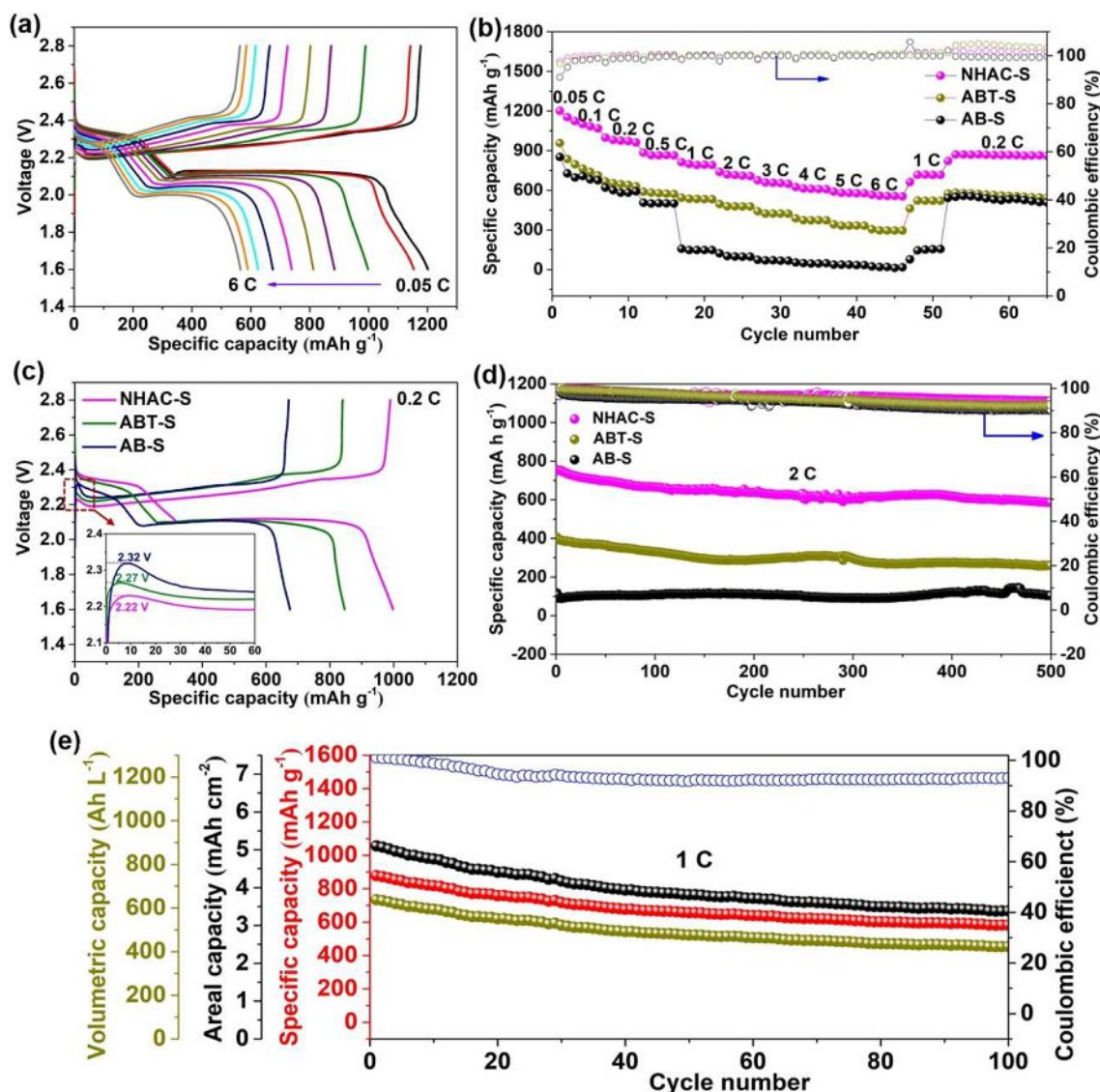


Figure 6. Fast, long-cycle and high mass loading cells: a) voltage-capacity profiles of the NHAC-S cathode and b) rate performance of NHAC-S, ABT-S and AB-S cathodes cycled at different rates. c) Voltage-capacity profiles of the three cathodes at 0.2 C and the inset of the potential barrier comparison of the cathodes; d) cycling performance at 2 C of three cathodes; e) cycling performance of NHAC-S cathode with a high sulfur loading of 5.8 mg cm⁻² at 1 C, and the corresponding areal and volumetric capacities.

ion transport rate under a very long cycling at a high current rate.

To realize the possibility of the high areal density cathode, high sulfur loading cathode (5.8 mg cm⁻²) at 1 C (9.7 mA cm⁻²) is also performed to verify the propelling and catalytic effect of the tunnels with polar sites. As shown in Figure 6e, the as-prepared cathode initially displays a high areal capacity of 5.1 mAh cm⁻² corresponding to volumetric capacity of 638 Ah L⁻¹. After 100 cycles, high reversible capacity 3.8 mAh cm⁻² (volumetric capacity of 423 Ah L⁻¹) can still remain, much higher than the majority works with biomass derived carbon.^[31,42–44]

To directly observe the catalytic effect of the tunnels on polysulfide conversions, the ex-situ SEM was also used to observe the surface morphology of the Li foils in the three cells

after 100 cycles at 0.5 C. As shown in Figure 7a, the counter Li foil in NHAC-S coin cell exhibits a relatively dense and smooth surface. While, obvious Li₂S particles can be easily seen in the ABT-S cell (Figure 7b) and it becomes much coarse in the AB-S cell (Figure 7c). This phenomenon might be attributed to the fact that the uncatalyzed/shuttled polysulfides react with metallic lithium to forms uneven Li₂S during the cycling process. EDS analysis on surface of Li foils in NHAC-S cell also shows the lowest sulfur content than the others (30 at% vs. 43 at% vs. 72 at%), which strongly confirms the polar catalytic sites and rapid ion tunnels in the carbon matrix in the NHAC-S cathode. The shuttle effect is also affirmed by the optical image of the separators in the three cells. As seen in Figure 7e, the separator in NHAC-S cell penetrates much less polysulfides than the ABT-S and AB-S cells (Figure 7f and g). These results indicate

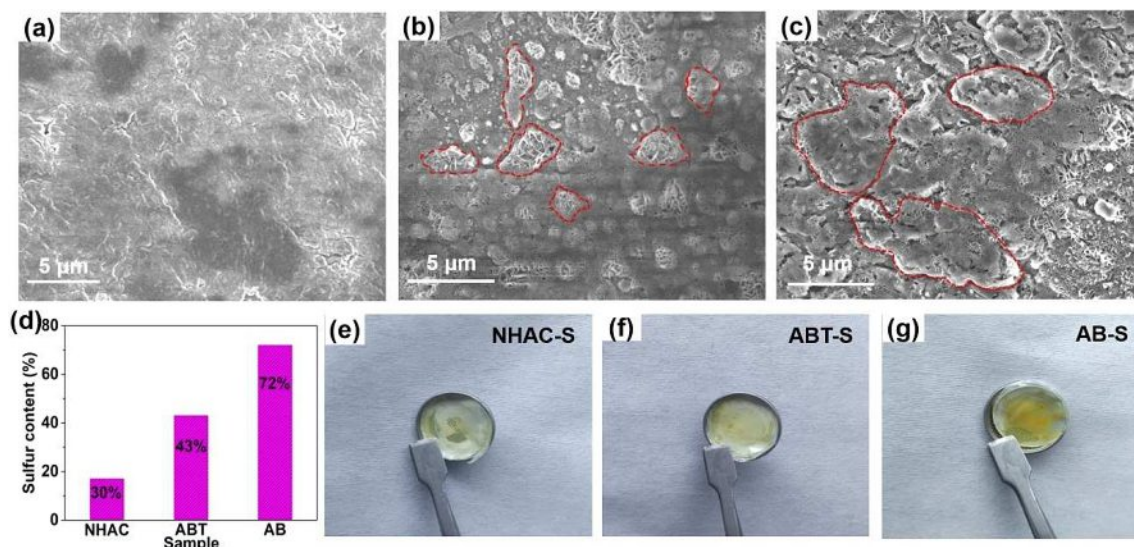


Figure 7. Inhibitory effect on shuttle effect: SEM image of the Li foil surface after 100 cycles at 0.5 C: a) NHAC-S; b) ABT-S; c) AB-S. d) Sulfur content on the surface of the Li foil detected by EDS analysis. The separators of the different cells after 100 cycles at 0.5 C: e) NHAC-S; f) ABT-S; g) AB-S.

the multi-functions of the ionic tunnels with polar active sites in improving lithium ion/electron transport and decreasing the energy barrier of interconversions among sulfur species synergistically to reach fast electrochemical reaction kinetics, thus contributing to the excellent high performances at high rate.

3. Conclusions

In summary, the electrochemical kinetics is highly improved through a functional tunnel with polar active sites to achieve a high-performance sulfur cathode. In such inherited structure, the porous ionic tunnels ensure the sufficient electrolyte infiltration and fast ion/electron transfer access to reach the active material. The large amount of polar heteroatom functional groups shows strong capability of catalyzing the conversions of polysulfides. Moreover, the energy barrier of interconversions among sulfur species is obviously decreased by catalytic sites without sacrificing the energy density of the cell. The as-synthesized NHAC-S cathode delivers a high discharge capacity of 564 mAh g^{-1} at 6 C and an excellent long cycling stability with a very low decay rates of 0.029% per cycle after 2000 cycles at 3 C. Even under high areal sulfur loading up to 5.8 mg cm^{-2} , a high initial areal capacity of 5.1 mAh cm^{-2} (high volumetric capacity of 638 Ah L^{-1}) at 1 C is achieved and a high reversible capacity 3.8 mAh cm^{-2} (volumetric capacity of 423 Ah L^{-1}) can still remain after 100 cycles, showing the great promising for practical utilization.

Experimental Section

Synthesis of Natural Heteroatom-Doped and Activated Carbon

The rice straw was washed with distilled water carefully for 3~5 times and dried at room temperature before use. The dried rice straw of 200 g with 50 mL distilled water was filled into 100 mL Teflon liners of stainless-steel autoclave, sealed and placed in a pre-heated oven at 180°C for 12 h. The treated straw was collected by filtration, dried overnight and then pyrolyzed at 800°C for 2 h under a flowing Ar atmosphere in a furnace. The pyrolyzed carbon were immersed into KOH solution with weight ratio of carbon to KOH of 1:2 under ultrasound and dried through a rapid evaporation process. The resultant was finally annealed at 800°C for 3 h under Ar gas flow for activation. The annealed product was washed with 1 mol L^{-1} HCl solution and then cleaned with distilled water repeatedly to remove the residual KOH and other impurities. Finally, the natural heteroatom-doped and activated carbon (NHAC) was collected by filtration and drying. The KOH activated acetylene black without carbon tunnels (named as AB) and with carbon tunnels (named as ABT) were prepared to verify the role of the tunnels in the cathode. The ABT was a physical mixture (mass ratio of 1:1) of KOH activated acetylene black with carbon tunnels made from the tube-like branches of the rice straw.

Preparation of Natural Heteroatom-Doped and Activated Carbon-Sulfur Composites

Sublimed sulfur (0.72 g) was added into a sodium sulfide solution ($1.82 \text{ g Na}_2\text{S} \cdot 9\text{H}_2\text{O}$ with 25 mL deionized water), with continuous stirring to generate homogeneous Na_2S_x solution. After the NHAC were dispersed into deionized water under ultrasound, Na_2S_x solution of 21 mL was dripped into the carbon suspension slowly with strong magnetic stirring. Then, HCOOH solutions with 2 mol L^{-1} was added dropwise to the suspending mixture for in-situ deposition of sulfur. Through stirring overnight, the as-deposited mixture was filtrated and washed by deionized water to remove the soluble impurities. The collection was fully dried and finally sealed in a vessel filled with argon gas and then annealed at 155°C

for 12 h to obtain NHAC–S composite. The ABT–S and AB–S composites were prepared following the same process.

Polysulfide Absorption Test

To prepare the polysulfides solution (0.2 mol L^{-1}), lithium sulfide of 92 mg with sublimed sulfur of 448 mg were dissolved into 10 mL mixed solvent of DME/DOL (1:1 in volume) by continuous stirring. Then, the samples for comparison with same mass were immersed into the diluted solution (5 mmol L^{-1}) for 8 h. The Li_2S_8 solutions in the supernatants were collected to detect the residual concentration, which were diluted by two times with DME/DOL solvent to enable the feasibility of ultraviolet visible (UV-vis) test. Preparation and dilution of solutions were all performed in an Ar-filled glovebox.

Preparation of Coin Cells

The carbon–sulfur composite with Super P and polyvinylidene fluoride (PVDF) binder were dispersed in N-methyl-2-pyrrolidone (NMP) solution according to a weight ratio of 7:2:1 under vigorous stirring to obtain homogenous slurry. The slurry was drop cast onto an aluminum foil current collector or Ni thin foam to form uniform cathode. The cathode was vacuum dried thoroughly before use. Coin cells (LIR2032) were assembled from the fabricated cathode film (circular disks of $\Phi 11 \text{ mm}$ with sulfur loading around 1.2 mg cm^{-2} to 5.8 mg cm^{-2}) with lithium foil as the anode separated by separator (Celgard 2400) in electrolyte/sulfur (E/S) ratio of $20 \mu\text{L mg}^{-1}$. The electrolyte (Suzhou China) comprises 1 mol L^{-1} LiTFSI and 1 wt% LiNO_3 in 1,3-dioxolane/1,2-dimethoxyethane solution (DOL/DME, 1:1 in volume). The cell was assembled inside a glove box ($\text{H}_2\text{O} \leq 0.5 \text{ ppm}$, $\text{O}_2 \leq 0.5 \text{ ppm}$, MBRAUN LAB-STAR) filled with argon gas.

Assembly of Symmetric Cells

Firstly, Li_2S (92 mg) and sulfur (320 mg) were dissolved into 10 mL electrolyte solution (1 mol L^{-1} LiTFSI and 1 wt% LiNO_3 in DOL/DME, 1:1 in volume) to generate 0.2 mol L^{-1} homogeneous Li_2S_6 solution under continuous stirring. Coin cells (2032-type) were assembled from the as-prepared pristine electrode film (NHAC, ABT and AB) as the cathode/anode separated by separator (Celgard 2400), using $40 \mu\text{L}$ of above synthesized polysulfide electrolyte as the mixed electrolyte in a glove box filled with highly pure Ar gas.

Nucleation of Lithium Sulfide

The Li_2S_8 solution is prepared through the same method of polysulfide adsorption test. Coin cells (2032-type) were assembled from the as-prepared pristine electrode film (NHAC, ABT and AB) as the cathode with Li foil anode separated by separator (Celgard 2400), using $30 \mu\text{L}$ of above synthesized polysulfide electrolyte with $10 \mu\text{L}$ solvent electrolyte. The assembled cells were potentiostatic discharged at 2.05 V for 6 h.

Materials and Cells Characterization

The X-ray diffraction (XRD) patterns were collected on an XRD-7000S X-ray diffractometer with Cu-K α radiation ($\lambda = 0.15418 \text{ nm}$) in a 2θ range from 10° to 80° . X-ray photoelectron spectra (XPS) were obtained from an ESCALAB 250XI system. Nitrogen absorption and desorption experiment was performed on ASAP 2020 Plus HD88 (Micromeritics). Thermal gravimetric analysis (TGA) was conducted on a TG/DTA 6200 setup with a heating rate of $10^\circ\text{C min}^{-1}$ under

nitrogen flow. Scanning electron microscopy (SEM) observation and energy dispersive spectra (EDS) elemental mapping were carried out using a Germany MERLIN Compact Scanning Electron Microscope (Zeiss Sigma HD). Transmission electron microscopy (TEM) samples were imaged using a Tecnai G2 F20S-TWIN Transmission Electron Microscope. Electrochemical measurements of the cells were carried out on a Neware Battery Testing System (BTS-5V 20 mA) within the voltage window of 1.6–2.8 V at different current rates. The electrochemical impedance spectroscopy (EIS), cyclic voltammetry (CV) and Li_2S nucleation test were performed with a VMP-3 potentiostat/galvanostat station (Germany).

Acknowledgements

This work was in part supported by the International Science and Technology Cooperation Program of China (2015DFR50350), the National Natural Science Foundation of China (No. 51771145), Shaanxi key R & D plan, international scientific and technological cooperation and exchange program (No. 2017KW-020), Shaanxi Natural Science Basic Research Plan (No. 2017JM5060). The authors are also grateful to the Instrument Analysis Center of Xi'an Jiaotong University for Nitrogen absorption and desorption measurement.

Conflict of Interest

The authors declare no conflict of interest.

Keywords: lithium–sulfur batteries · functional ion tunnels · fast reaction kinetics · catalytic effects · high rate

- [1] S. Ma, L. Wang, Y. Wang, P. Zuo, M. He, H. Zhang, L. Ma, T. Wu, G. Yin, *Carbon* **2019**, *143*, 878–889.
- [2] H. Wu, Y. Li, J. Ren, D. Rao, Q. Zheng, L. Zhou, D. Lin, *Nano Energy* **2019**, *55*, 82–92.
- [3] M. Wang, L. Fan, X. Wu, Y. Qiu, Y. Wang, N. Zhang, K. Sun, *Chem. Eur. J.* **2019**, *25*, 5416–5421.
- [4] R. Fang, S. Zhao, Z. Sun, D. W. Wang, H. M. Cheng, F. Li, *Adv. Mater.* **2017**, *29*, 1606823.
- [5] K. Sun, A. K. Matarasso, R. M. Epler, X. Tong, D. Su, A. C. Marschilok, K. J. Takeuchi, E. S. Takeuchi, H. Gan, *J. Electrochem. Soc.* **2018**, *165*, A416–A423.
- [6] H. Wu, L. Xia, J. Ren, Q. Zheng, C. Xu, D. Lin, *J. Mater. Chem. A* **2017**, *5*, 20458–20472.
- [7] J. Ren, Y. Zhou, L. Xia, Q. Zheng, J. Liao, E. Long, F. Xie, C. Xu, D. Lin, *J. Mater. Chem. A* **2018**, *6*, 13835–13847.
- [8] W. Ai, W. Zhou, Z. Du, Y. Chen, Z. Sun, C. Wu, C. Zou, C. Li, W. Huang, T. Yu, *Energy Storage Mater.* **2017**, *6*, 112–118.
- [9] X. Ding, X. Pan, N. Liu, L. Li, X. Wang, G. Xu, J. Yang, J. Yang, N. Yu, M. Liu, W. Li, Y. Zhang, *Chem. Eur. J.* **2019**, *25*, 3775–3780.
- [10] L. Li, L. Chen, S. Mukherjee, J. Gao, H. Sun, Z. Liu, X. Ma, T. Gupta, C. V. Singh, W. Ren, H. M. Cheng, N. Koratkar, *Adv. Mater.* **2017**, *29*, 1602734.
- [11] M. Cheng, H. Zhao, Z. Zhao, J. Wang, L. Cao, H. Zhang, X. Duan, C. Wang, J. Wang, J. Wang, C. Lu, *Green Chem.* **2018**, *20*, 4675–4683.
- [12] L. Xia, Y. Zhou, J. Ren, H. Wu, D. Lin, F. Xie, W. Jie, K. H. Lam, C. Xu, Q. Zheng, *Energy Fuels* **2018**, *32*, 9997–10007.
- [13] M. Ren, X. Lu, Y. Chai, X. Zhou, J. Ren, Q. Zheng, D. Lin, *J. Colloid Interface Sci.* **2019**, *552*, 91–100.
- [14] Z. Song, X. Lu, Q. Hu, J. Ren, W. Zhang, Q. Zheng, D. Lin, *J. Power Sources* **2019**, *421*, 23–31.
- [15] J. Ren, Y. Zhou, H. Wu, F. Xie, C. Xu, D. Lin, *J. Energy Chem.* **2019**, *30*, 121–131.

- [16] Z. Fan, B. Ding, H. Guo, M. Shi, Y. Zhang, S. Dong, T. Zhang, H. Dou, X. Zhang, *Chem. Eur. J.* **2019**, *25*, 1–9.
- [17] Y. Zhong, D. Chao, S. Deng, J. Zhan, R. Fang, Y. Xia, Y. Wang, X. Wang, X. Xia, J. Tu, *Adv. Funct. Mater.* **2018**, *28*, 1706391.
- [18] J. Zhang, H. Huang, J. Bae, S. H. Chung, W. Zhang, A. Manthiram, G. Yu, *Small Methods* **2018**, *2*, 1700279.
- [19] J. Zhang, C. You, J. Wang, H. Xu, C. Zhu, S. Guo, W. Zhang, R. Yang, Y. Xu, *Chem. Eng. J.* **2019**, *368*, 340–349.
- [20] J. Zhang, C. You, W. Zhang, J. Wang, S. Guo, R. Yang, Y. Xu, *Electrochim. Acta* **2017**, *250*, 159–166.
- [21] Z. W. Seh, Y. Sun, Q. Zhang, Y. Cui, *Chem. Soc. Rev.* **2016**, *45*, 5605–5634.
- [22] J. L. Gómez-Urbano, J. L. Gómez-Cámer, C. Botas, T. Rojo, D. Carriazo, *J. Power Sources* **2019**, *412*, 408–415.
- [23] J. Wang, S. Cheng, W. Li, S. Zhang, H. Li, Z. Zheng, F. Li, L. Shi, H. Lin, Y. Zhang, *J. Power Sources* **2016**, *321*, 193–200.
- [24] M. Yu, J. Ma, M. Xie, H. Song, F. Tian, S. Xu, Y. Zhou, B. Li, D. Wu, H. Qiu, R. Wang, *Adv. Energy Mater.* **2017**, *7*, 1602347.
- [25] J. Wang, S. Cheng, W. Li, L. Jia, Q. Xiao, Y. Hou, Z. Zheng, H. Li, S. Zhang, L. Zhou, M. Liu, H. Lin, Y. Zhang, *Nano Energy* **2017**, *40*, 390–398.
- [26] J. Yang, J. Xie, X. Zhou, Y. Zou, J. Tang, S. Wang, F. Chen, L. Wang, *J. Phys. Chem. C* **2014**, *118*, 1800–1807.
- [27] S. Xu, C. Chen, Y. Kuang, J. Song, W. Gan, B. Liu, E. M. Hitz, J. W. Connell, Y. Lin, L. Hu, *Energy Environ. Sci.* **2018**, *11*, 3231–3237.
- [28] D. Guo, R. Shibuya, C. Akiba, S. Saji, T. Kondo, J. Nakamura, *Science* **2016**, *351*, 361–365.
- [29] J. Sun, S. E. Lowe, L. Zhang, Y. Wang, K. Pang, Y. Wang, Y. Zhong, P. Liu, K. Zhao, Z. Tang, H. Zhao, *Angew. Chem. Int. Ed.* **2018**, *130*, 16749–16753.
- [30] L. Jia, J. Wang, Z. Chen, Y. Su, W. Zhao, D. Wang, Y. Wei, K. Jiang, J. Wang, Y. Wu, J. Li, W. Duan, S. Fan, Y. Zhang, *Nano Res.* **2019**, *12*, 1105–1113.
- [31] X. Wu, L. Fan, M. Wang, J. Cheng, H. Wu, B. Guan, N. Zhang, K. Sun, *ACS Appl. Mater. Interfaces* **2017**, *9*, 18889–18896.
- [32] Q. Pang, J. Tang, H. Huang, X. Liang, C. Hart, K. C. Tam, L. F. Nazar, *Adv. Mater.* **2015**, *27*, 6021–6028.
- [33] N. Deng, J. Ju, J. Yan, X. Zhou, Q. Qin, K. Zhang, Y. Liang, Q. Li, W. Kang, B. Cheng, *ACS Appl. Mater. Interfaces* **2018**, *10*, 12626–12638.
- [34] F. Xu, S. Yang, G. Jiang, Q. Ye, B. Wei, H. Wang, *ACS Appl. Mater. Interfaces* **2017**, *9*, 37731–37738.
- [35] H. Lin, L. Yang, X. Jiang, G. Li, T. Zhang, Q. Yao, G. W. Zheng, J. Y. Lee, *Energy Environ. Sci.* **2017**, *10*, 1476–1486.
- [36] J. Wang, L. Jia, J. Zhong, Q. Xiao, C. Wang, K. Zang, H. Liu, H. Zheng, J. Luo, J. Yang, H. Fan, W. Duan, Y. Wu, H. Lin, Y. Zhang, *Energy Storage Mater.* **2018**, *18*, 246–252.
- [37] F. Y. Fan, W. C. Carter, Y. M. Chiang, *Adv. Mater.* **2015**, *27*, 5203–5209.
- [38] H. Al Salem, G. Babu, C. V. Rao, L. M. Arava, *J. Am. Chem. Soc.* **2015**, *137*, 11542–11545.
- [39] G. Babu, N. Masurkar, H. Al Salem, L. M. Arava, *J. Am. Chem. Soc.* **2017**, *139*, 171–178.
- [40] Q. Wang, N. Tian, K. Xu, L. Han, J. Zhang, W. Zhang, S. Guo, C. You, *J. Alloys Compd.* **2016**, *686*, 267–272.
- [41] M. Thakurathi, E. Gurung, M. M. Cetin, V. D. Thalangamaarachchige, M. F. Mayer, C. Korzeniewski, E. L. Quitevis, *Electrochim. Acta* **2018**, *259*, 245–252.
- [42] F. Ai, N. Liu, W. Wang, A. Wang, F. Wang, H. Zhang, Y. Huang, *Electrochim. Acta* **2017**, *258*, 80–89.
- [43] X. L. You, L. J. Liu, M. Y. Zhang, M. D. Walle, Y. Li, Y. N. Liu, *Mater. Lett.* **2018**, *217*, 167–170.
- [44] Y. Zhong, X. Xia, S. Deng, J. Zhan, R. Fang, Y. Xia, X. Wang, Q. Zhang, J. Tu, *Adv. Energy Mater.* **2018**, *8*, 1701110.

Manuscript received: August 15, 2019

Revised manuscript received: September 4, 2019

Accepted manuscript online: September 17, 2019